JOURNAL OF MATERIALS SCIENCE **33** (1998) 4961–4969

Microstructure development in laser-processed Al–Ti–Ni alloys with 25 at. % Ti

A. E. GUNNÆS, A. OLSEN, J. TAFTØ
Centre for Materials Science/Department of Physics, University of Oslo, Gaustadalleen 21, 0371 Oslo, Norway

The microstructure of laser-processed $(Al_{1-x}Ni_x)_3$ Ti with Ni content ranging from 5 to 15 at. % has been studied by scanning-and transmission-electron microscopy (SEM and TEM). All samples contain Al-rich dendrites with Ni-rich interdendritic phases. The dendrites in the 5 at. % Ni alloy consist of the Al_3Ti phase with the DO_{22} type structure, whereas the alloys containing 8 to 15 at. % Ni consist of the $Al_{67}Ni_8Ti_{25}$ phase with the $L1_2$-type structure. The lattice parameter of the $L1_2$ type structure of $Al_{67}Ni_8Ti_{25}$ was determined by comparing the Higher Order Laue Zone (HOLZ) line patterns in experimental and calculated convergent beam electron diffraction disks. The lattice parameter was found to be $a = 0.3935 \pm 0.0003$ nm. Within the $L1_2$ type regions of the alloy with 8 at. % Ni, precipitates with a new primitive tetragonal structure was found. The cell dimensions are $a = 0.39$ nm and $c = 1.18$ nm. $AlNTi_2$ with Ti : Al ratio equal to 2.0 ± 0.2 was found as needles in interdendritic regions. The cell dimensions are consistent with $a = 0.299$ nm and $c = 1.361$ nm and space group $P6_3/mmc$.

1. Introduction

The intermetallic alloy Al_3Ti has been considered as a potential material for low-density, high-temperature structural applications due to its density (3.3 g/cm^3) and relatively high melting point (1340 °C) [1]. The high aluminium content in Al_3Ti results in a much better oxidation resistance than AlTi [2]. Unfortunately the tetragonal Al_3Ti is brittle [3]. During the last 10 years a large amount of papers have been related to macroalloying with various transition elements M (M = V, Cr, Mn, Fe, Co, Ni, Cu, Zn, Rh, Pd, Ag, Pt and Au) in order to change the DO_{22} structure into a high symmetry $L1_2$ type structure [4–10]. Even though transformation from the tetragonal DO_{22} structure into the high-symmetry cubic $L1_2$ structure is achieved, Al_3Ti remains brittle in tension and shows brittle transgranular cleavage type in the fracture mode [11]. High antiphase boundary (APB) energy on the (1 1 1) plane for trialuminide alloys, which is attributed to the directional nature of d-electrons in Ti_d–Al_p bonding [12], prevents the formation of slip systems.

The most common way to produce these macroalloyed Ti aluminides has been conventional casting, arc melting, or induction melting as reviewed by Feest and Tweed [13]. In 1992 Ma *et al.* [14] showed that macroalloyed Ti aluminides could be produced by a laser-process route. This route was found efficient and convenient for processing small amounts of intermetallic materials. Ma *et al.* [14] studied the microstructure of three different laser-processed Al–Ti alloys. The macroalloying elements in these alloys were Cu, Fe and Ni, and the composition of the alloys was Al_5Ti_2M (M = Cu, Fe and Ni). Samples, as laser processed, were investigated by use of optical microscopy, whereas samples annealed at 1000 °C for 100 h were investigated by both optical and TEM.

Very few results from intermetallic materials produced by the laser process route have been reported after Ma *et al.* [14] described the route in 1992. In order to get more information about the process route and the direct response of the laser process on the microstructure of the aluminides, a series of Al–Ni–Ti alloys with 25 at. % Ti was produced in the present work. Al-rich Al–Ni–Ti alloys have previously been processed by more conventional techniques [10, 15–17] and the findings of the present investigation will therefore be compared to these. The microstructure of the laser-processed alloys was in the present study investigated by combining analytical SEM and analytical TEM.

2. Experimental

2.1. Material

Five different Al–Ni–Ti alloys with 25 at. % Ti were investigated in the present study. The composition of the alloys is shown in Table I. Fig. 1 shows an isothermal section of the Al–Ni–Ti-phase diagram at 800 °C based on the phase diagram of Raman *et al.* [18]. The compositions of the processed alloys are lying along the straight line with 25 at. % Ti crossing the DO_{22}, DO_{23} and $L1_2$ phase field. Alloy C is lying in the middle of the $L1_2$ phase field with Alloy A and B on the right-hand side and Alloy D and E on the left-hand side.

The starting material for the alloys was pure metal powder of Al 99.9% purity, and powders of Ni and Ti both with less than 0.5% impurities. The desired

TABLE I The composition of the Al–Ni–Ti alloys studied given in at. %

	Alloy A	Alloy B	Alloy C	Alloy D	Alloy E
Al	70	67	65	62.5	60
Ni	5	8	10	12.5	15
Ti	25	25	25	25	25

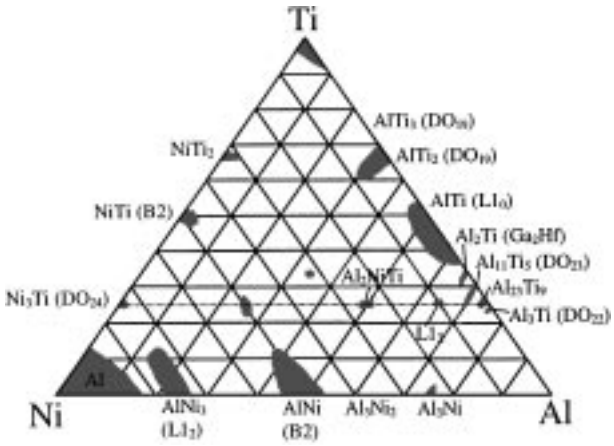

Figure 1 Isothermal section of the Al–Ni–Ti-phase diagram at 800 °C [18].

amount of the metal powders was mixed by blending in air. The powders were then cold compressed using a Carver Laboratory Compressor to form disks with 22-mm diameter and 2-mm height. During the cold-pressing the pressure was 2600 kg/cm^2 and the condensing ratio was about 75%.

2.2. Laser processing route

The disks of cold-pressed powders were placed on a polished brass mirror with four screws keeping the disk steady during the laser process. The brass mirror was polished in order to reflect the heat radiation and thus reduce the heat absorption of the brass. The laser beam from a 10 kW fast transverse flow United Technologies CO_2-laser was focused through a laser integrator onto an area of 12 × 12 mm^2 on the disk as illustrated in Fig. 2. The power of the laser beam was varied from

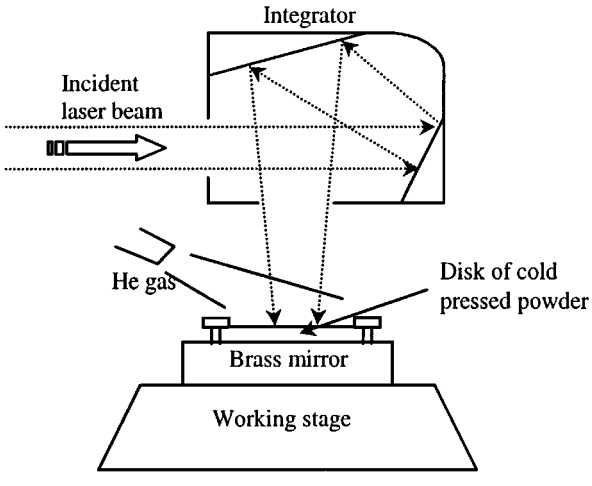

Figure 2 Diagram of the laser processing of the aluminides.

5 to 6 kW and the illumination time between 5 and 30 seconds depending on the response of the material. This differs somewhat from the parameters of Ma *et al.* [14] who used only 6 kW effect and an illumination time of 5 seconds. During the laser processing a side nozzle blew He onto the disk, thereby reducing the absorption of light by ionised gases and preventing high-temperature oxidation.

When the disks cooled down, the previously illuminated areas formed an intermetallic material. Because the circular area of the cold-pressed powder (380 mm^2) is larger than the quadratic illuminated area (144 mm^2), parts of the disks were not illuminated and consequently not melted. The main focus in the present investigation has been placed on the central part of the illuminated areas, where all the elements have been in the liquid phase before solidifying. More peripheral parts of the disks were avoided because the low energy density from the laser resulted in incomplete melting of the material.

2.3. Experimental techniques

Polished samples from the alloys were investigated by use of a Philips 30 XL SEM equipped with an EDAX X-ray energy dispersive system. The X-ray energy dispersive spectroscopy (EDS) spectra obtained in the SEM were analysed quantitatively by correcting for X-ray yield, detector efficiency, absorption and fluorescence effects. The phases present in the alloys were studied by detecting the backscattered electrons (BSE) where different phases are seen with different contrast depending on the average atomic number in the phases. The Al-rich phases gave rise to the darkest image because Al has the lowest atomic number (13) of the elements present. Ni-rich areas gave rise to the brightest image because it has the highest atomic number (28). In order to study the distribution of the elements, images were formed by detecting characteristic X-ray lines during the scanning sequence (elemental mapping).

TEM samples from the alloys were prepared by grinding and ion thinning in a Gatan dual ion-mill. The TEM work was performed at 200 kV in a JEOL 2000 FX equipped with Tracor Northern X-ray detector and a SCANDNORDAX X-ray analyser. The microstructure of the phases was studied using a combination of EDS, electron energy loss spectroscopy (EELS), selected area diffraction (SAD), convergent beam electron diffraction (CBED), bright and dark field imaging (BF/DF) and high resolution electron microscopy (HREM).

3. SEM observations

Fig. 3 shows a series of overview BSE images from central parts of the alloys. It is clear that none of the samples are single-phase materials. All the samples contain Al-rich dendrites with Ni-rich interdendritic phases. The dendrite structure of the fully melted part in the alloys was, however, found to vary within a sample. It is well known that the dendrite arm spacing can be related to the solidification rate. This variation of microstructure indicates that the solidification rate varied inside the

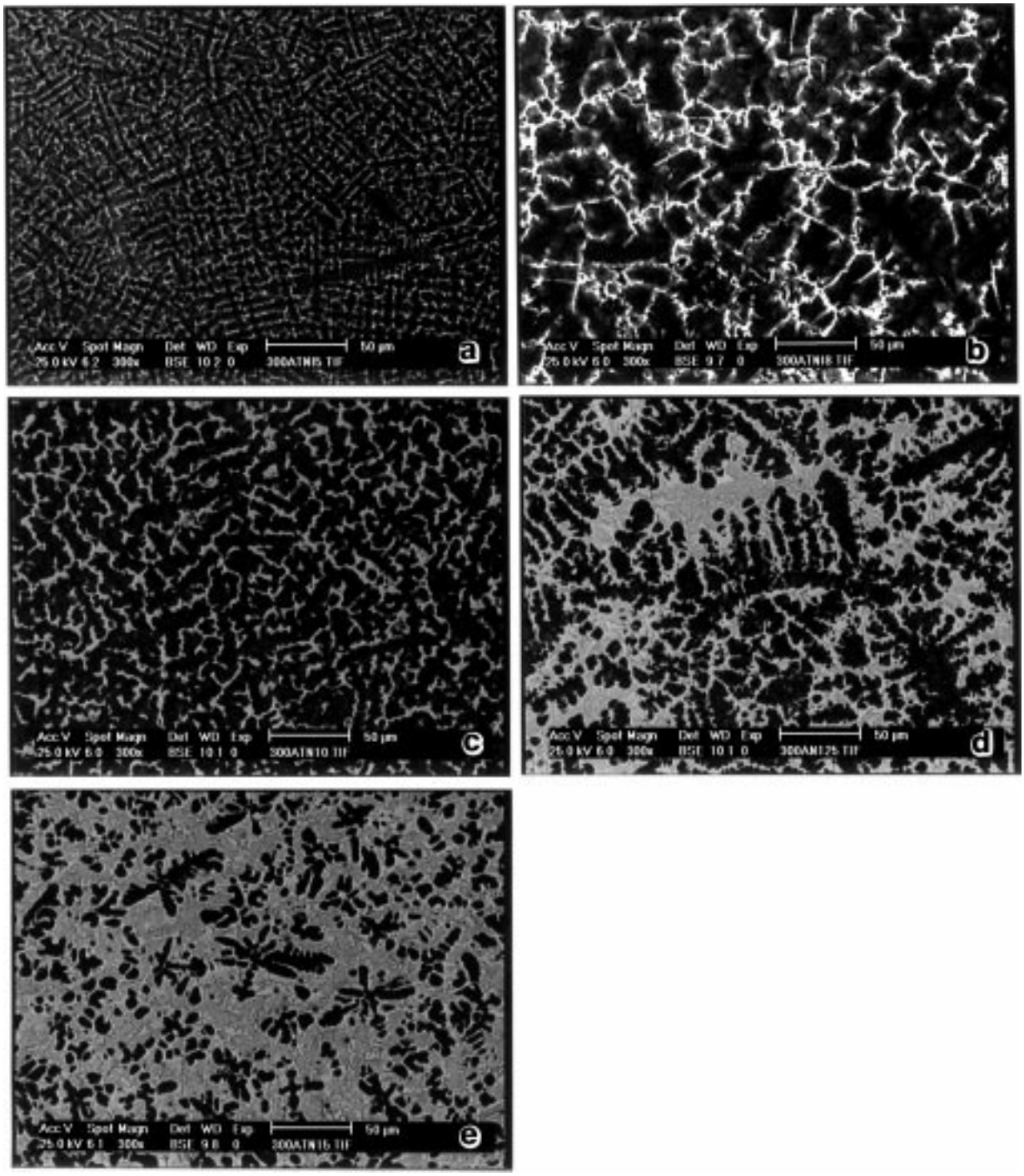

Figure 3 BSE micrograph showing the microstructure of the central part of the Al–Ti–Ni alloys with (a) 5 (Alloy A), (b) 8 (Alloy B), (c) 10 (Alloy C), (d) 12.5 (Alloy D) and (e) 15 at. % Ni (Alloy E).

illuminated and subsequently melted area of the disks. The dendrite arm spacing is between 5 and 10 μm in the areas shown in Fig. 3. According to the theory of dendrite formation, see e.g. [19], the cooling rate in these areas has been around 10^3 K/s, which is inside the range of what is called rapid solidification.

The dendrites in the alloys with 5, 8 and 10 at. % Ni (Alloy A, B and C) show lighter coloured shades in the outer part of the dendrite arms (Fig. 3a–c). This colour change indicates an increase in Ni content in the outer parts of the dendrite arms. The increase in Ni content was confirmed by EDS. The average compositions of the central part of the dendrites in Alloy A, B and C were found to be $Al_{69}Ti_{28}Ni_3$, $Al_{68}Ti_{28}Ni_4$ and $Al_{66}Ti_{26}Ni_8$ respectively. In the outer parts of the dendrites the Ni content had increased and the average compositions were found to be $Al_{70}Ti_{25}Ni_5$, $Al_{67}Ti_{25}Ni_8$ and $Al_{65}Ti_{24}Ni_{11}$ in Alloy A, B and C respectively (Table II). The composition of the dendrites in Alloy D and E (Fig. 3d and e) was found to be uniform. The average compositions of these alloys were $Al_{67}Ti_{25}Ni_8$ and $Al_{66}Ti_{26}Ni_8$ as given in Table II.

The interdendritic regions in all the alloys consist of several phases. Fig. 4 shows close-up BSE micrographs of the interdendritic phases in (a) Alloy B and (b) Alloy E. As can be seen in Fig. 4a, the interdendritic phases in Alloy B consist of three different intermetallic phases marked as a, b and c. The interdendritic phases

TABLE II Average compositions of the phases in the Al–Ti–Ni alloys found by EDS in the SEM

	Alloy A			Alloy B			Alloy C			Alloy D			Alloy E		
	Al	Ti	Ni	Al	Ti	Ni	Al	Ti	Ni	Al	Ti	Ni	Al	Ti	Ni
Dendrite (central)	69	28	3	68	28	4	66	26	8						
Dendrite (outer p.)	70	25	5	67	25	8	65	24	11	67	25	8	66	26	8
Segregation	70	19	11	63	18	19	61	21	18						
Segregation (bright)										59	22	19	57	22	21
Segregation (dark)													53	31	16

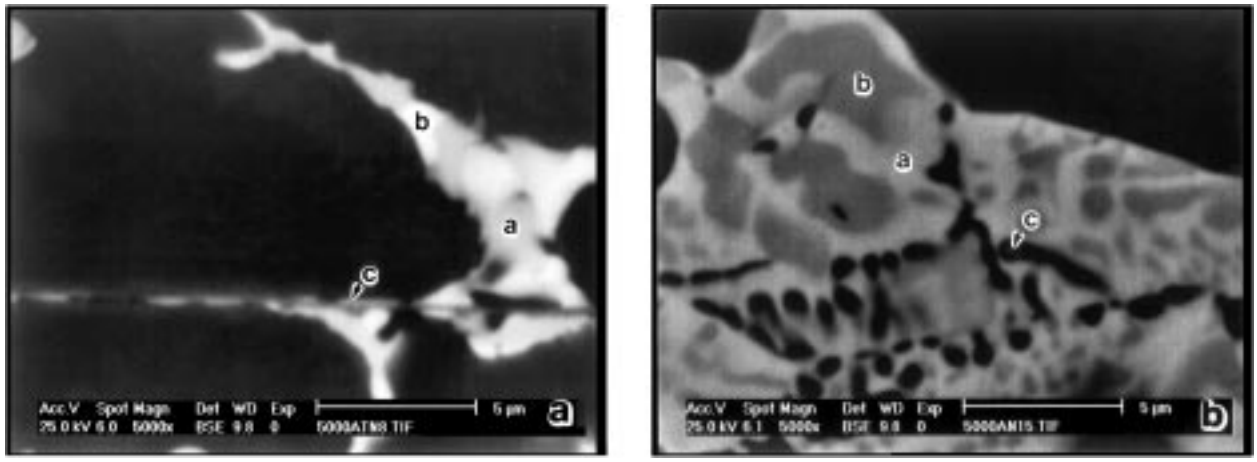

Figure 4 BSE micrograph showing microsegregation in (a) Alloy B and (b) Alloy E.

in Alloy A and C were mainly found to consist of two different intermetallic phases. The long, needle-shaped phase marked as c in Fig. 4a was not seen to a large extent in Alloy A and C. The average composition of the interdendritic phases in Alloy A, B and C from EDS analyses (Table II) shows that the Ti:Ni ratio is approximately 2 in Alloy A and 1 in both Alloy B and C. This indicates that the interdendritic phase in Alloy A is of a different kind than the interdendritic phases found in Alloy B and C. One should, however, keep in mind that bulk analyses of small particles in SEM may be strongly affected by surrounding regions.

In Fig. 4a some small black particles can be seen. Because light elements give rise to low intensity in BSE images, these particles may be rich in oxygen as reported by Ma *et al.* [14]. It is expected that these oxides are introduced as a result of unavoidable oxidised-powder surfaces and small-scale oxidation during the laser melting in spite of the applied He gas.

The interdendritic regions in Alloy D and E are of similar kind. The BSE micrograph of Alloy E in Fig. 4b shows that the matrix consists of three intergrown phases. The light gray areas labelled a in Fig. 4b have about the same compositions as the interdendritic phases in Alloy B and C (Table II). The dark gray areas marked as b in Fig. 4b were found to have an average composition of $Al_{53}Ti_{31}Ni_{16}$. In Alloy D the dark gray areas were too small to give any reliable EDS result. The contrast was, however, very similar to the dark-gray areas in Alloy E, indicating the presence of the same phase. In addition to these two types of areas a third type is seen in both Alloy D and E. In Fig. 4b the third type of area, marked as c, has similar contrast as the neighbouring dendrite. EDS analyses from larger areas of this kind show similar compositions as the dendrites in the alloys, indicating the presence of the same phases.

4. Identification and description of the phases encountered in TEM

The composition of the dendrites in Alloy A (Table II) is very close to the phase region of $Al_{11}Ti_5$ with the DO_{23} type structure (Fig. 1). However, this phase was not found in any of the alloys in the present TEM investigation. With TEM the structure of the dendrites in Alloy A was found by SAD to have the DO_{22} type structure of Al_3Ti. Al_3Ti has the space group I4/mmm and cell dimensions $a = 0.3848$ nm and $c = 0.8596$ nm [20]. The dendrites in Alloy B–E were found to have the $L1_2$ structure of $Al_{67}Ni_8Ti_{25}$ with the space group Pm 3 m.

4.1. Lattice parameter determination of the $L1_2$ structure

Various lattice parameters have been published of the Ni-modified $L1_2$ structure after Schubert *et al.* [21] reported its existence in 1964. In the first X-ray work by Schubert *et al.* the lattice parameter was found to be $a = 0.394$ nm [21]. In a second paper of Raman *et al.* in 1965 [18] the lattice parameter was reported to be $a = 0.393$ nm. In recent years Turner *et al.* [16], Durlu and Inal [22] and Ma *et al.* [14] reported lattice parameter $a = 0.395$ nm, $a = 0.3935 \pm 0.0004$ nm and $a = 0.390 \pm 0.002$ nm, respectively. The work by Turner *et al.* [16] and Durlu and Inal [22] is based on X-ray diffraction whereas the work by Ma *et al.* [14] is based on SAD patterns calibrated with standard gold specimen.

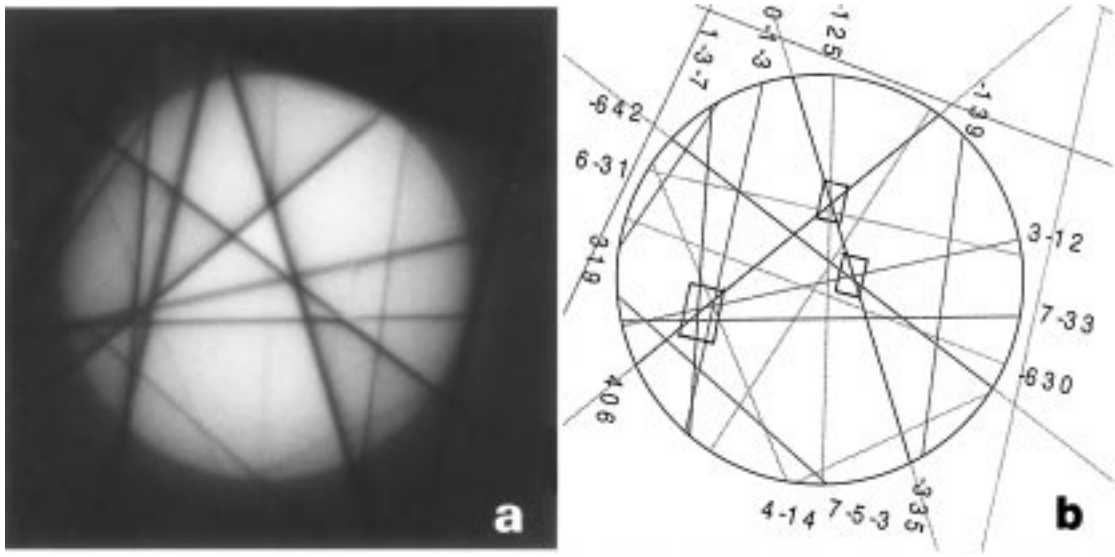

Figure 5 (a) Experimental CBED pattern from the $L1_2$ structure close to the $[\bar{2}\,\bar{4}\,1]$ zone axis and (b) corresponding calculated CBED pattern with $a = 0.3935$ nm and 203.2 kV.

In order to determine the lattice parameter of the $L1_2$ structure in the present study, a lattice parameter determination technique for TEM was used. This technique is based on sensitive triangles of Higher Order Laue Zones (HOLZ) and Kikuchi lines [23, 24]. The accuracy of the method is better than 0.1% and can be used on small crystal areas.

The high voltage of the microscope, and thus the wavelength of the electrons, has to be known with high accuracy in order to determine the lattice parameter. This was done by comparing the HOLZ lines in a CBED central disk from pure silicon with kinematical calculated patterns. The experiment was performed at room temperature and the lattice parameter $a = 0.543095$ nm for Si was used in the calculations [25]. Strong dynamical regions of the CBED pattern were avoided by choosing high index zone axes. By using this method the high voltage of the microscope was determined to be 203.2 ± 0.2 kV, and the corresponding wavelength of the electrons 0.002485 ± 0.000001 nm. The determination of the high voltage and the lattice parameter of the $L1_2$ structure were performed during the same TEM session to avoid variations in the high voltage.

Fig. 5a shows an experimental CBED pattern close to the $[\bar{2}4\ 1]$ zone axis from the $L1_2$ structure in Alloy E. To compare the positions of the HOLZ lines in the experimental and calculated CBED pattern, three sensitive triangles were used. These are marked in Fig. 5. By comparing the sensitive triangles in the experimentally CBED pattern with corresponding triangles in calculated CBED patterns, the best fit was found with a lattice parameter of $a = 0.3935 \pm 0.0003$ nm as seen in Fig. 5b. This is consistent with the lattice parameter reported by Durlu and Inal [22] and close to the values 0.394 nm and 0.393 nm as reported by Schubert *et al.* [21] and Raman *et al.* [18].

4.2. Precipitation in the $L1_2$ structure

The composition of the dendrites was found to vary inside single grains in Alloy B. In regions with less than 8 at. % Ni, small precipitates and GP zones were observed (Fig. 6). The density and the size of the precipitates were found to vary with composition. In the outer part of the dendrites containing 8–10 at. % Ni, no precipitates were found. As shown in the [0 0 1] SAD pattern in Fig. 7a, only diffraction spots from the $L1_2$ structure could be seen in these regions. The regions with GP zones (Fig. 6) exhibit streaks along the ⟨100⟩ directions as seen in the SAD pattern shown in Fig. 7b. In the central part of the dendrites with 4–5 at. % Ni large precipitates were found. These precipitates give rise to diffraction spots as can be seen in Fig. 7c. From SAD tilting series the crystal structure of the precipitates was found to be primitive tetragonal with the approximate

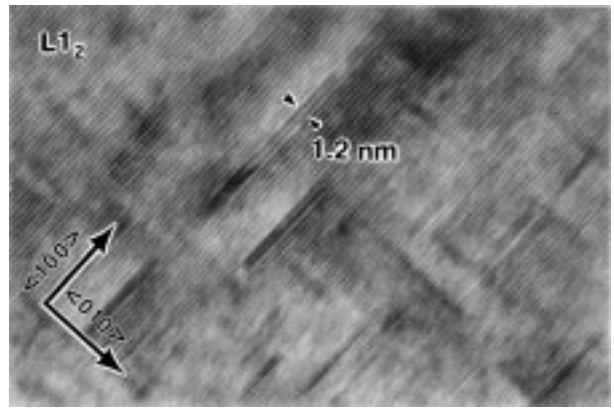

Figure 6 HREM image showing small precipitates (GP-zones) in the $L1_2$ structure in Alloy B.

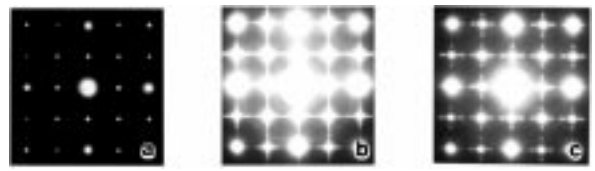

Figure 7 [0 0 1] SAD patterns from the $L1_2$ structure showing (a) no evidence of precipitates, (b) diffuse streaks along the ⟨100⟩ directions from GP zones and (c) diffraction spots from larger precipitates.

cell dimensions a = 0.39 nm and c = 1.18 nm. This phase has not been reported previously by others.

4.3. Interdendritic phases in Alloy A–E

In alloy A the interdendritic phases as seen in Fig. 3a were found mainly to consist of the Al_3Ni phase. The Al_3Ni phase is orthorhombic with space group Pnma and cell dimensions a = 0.66114 nm, b = 0.73662 nm and c = 0.48117 nm [26].

The interdendritic regions in Alloy B, C, D and E were found mainly to consist of the Al_2NiTi phase. The Al_2TiNi phase is cubic with the space group $Fm\bar{3}m$ and the cell dimension a = 1.190 nm [14, 18]. In addition to the Al_2NiTi phase the interdendritic regions in Alloy B and C were found to consist of the AlNi phase. This phase has the space group $Pm\bar{3}m$ and cell dimension a = 0.28864 nm [27].

The interdendritic regions in Alloy D and E were found to consist of the Al_3NiTi_2 phase in addition to Al_2NiTi. These phases were found to grow closely together as seen in Fig. 8. The Al_3NiTi_2 phase is hexagonal with space group $P6_3/mmc$ and cell dimensions a = 0.498 and c = 0.812 nm [21, 28]. The small dark areas as seen in the SEM study (Fig. 4b) were found by TEM to consist of the $L1_2$ structure.

4.4. $AlNTi_2$

The needle-shaped phase clearly seen by SEM in Alloy B was found in all the alloys B–E by using TEM. Fig. 9

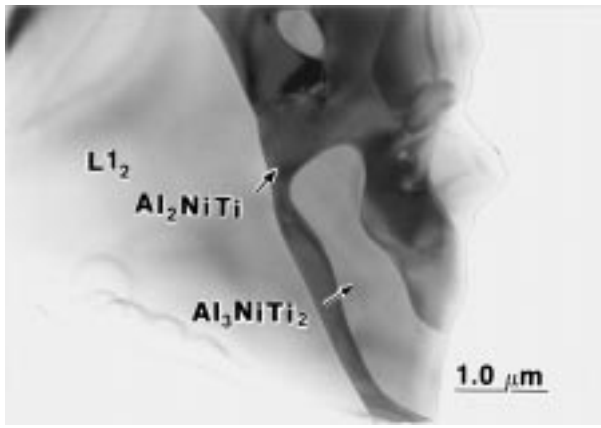

Figure 8 BF image from Alloy E showing intergrowing areas of Al_2NiTi and Al_3NiTi_2 close to a dendrite.

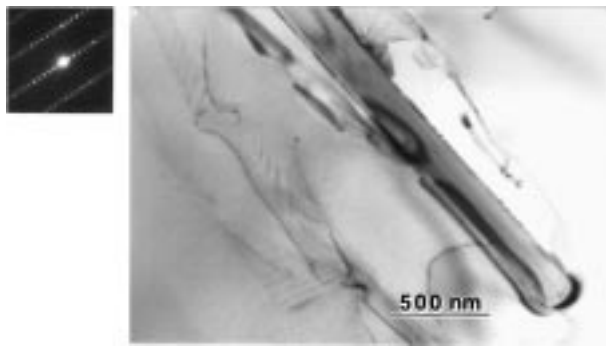

Figure 9 BF image showing a $AlNTi_2$ needle with hollow core and a dislocation in the tip with the corresponding SAD pattern.

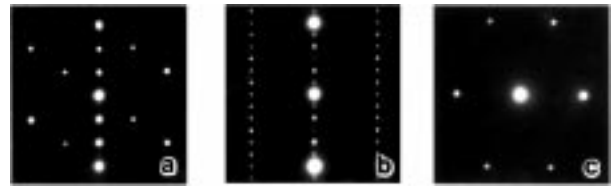

Figure 10 SAD patterns from the $AlNTi_2$ needles; (a) 001 row and $[0\,1\,\bar{1}]_{L1_2}$, (b) [1 1 0] and (c) [4 4 1] projection.

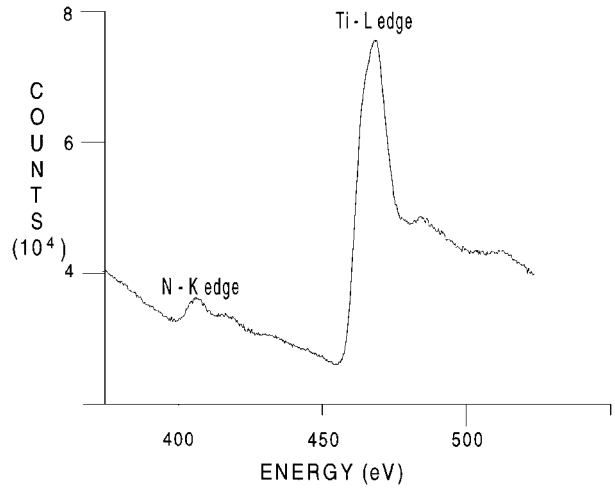

Figure 11 EELS spectrum from an $AlNTi_2$ needle in Alloy B.

shows a BF image of a needle in Alloy B with the corresponding SAD pattern. From the EDS analyses in the TEM the needles were found to contain Ti and Al with the Ti : Al ratio 2.0 ± 0.2. From SAD patterns (Fig. 10) the needles were found to have a primitive hexagonal Bravais lattice with cell dimensions $a = 0.299$ nm and $c = 1.361$ nm. Fig. 10a shows the $[0\,1\,\bar{1}]$ SAD pattern from the $L1_2$ structure together with the 001 row of the Al–Ti phase where the ⟨001⟩ direction of Al–Ti is parallel to the ⟨111⟩ direction of $L1_2$. Fig. 10b and c show the $[1\,\bar{1}\,0]$ and [4 4 1] projection of the Al–Ti phase, respectively. The c-axis is perpendicular to the growth direction as seen in Fig. 9. The space group of the phase has been found to be consistent with $P6_3/mmc$. The structure has a screw axis along the c-axis which can be recognised in the SAD patterns in Fig. 10a and b where the reflection condition is: 001, 1 = 2n.

The structure of the present phase is not reported for binary Al–Ti phases but is, however, known for ternary Al–Ti phases containing either N or C [28]. The structure type of $AlNTi_2$ and $AlCTi_2$ is $AlCCr_2$ [29] where the Ti atoms occupy the 4f positions and the Al and N atoms occupy the 2d and 2a positions, respectively. Because C and N could not be detected in the EDS analysis, EELS was carried out. Fig. 11 shows an EELS spectrum taken from a needle in Alloy B. The needles contain N, which confirms that the needles are not a new Al–Ti phase but the ternary $AlNTi_2$ phase.

5. Discussion

All the different phases found in the present study are summarised in Table III. According to the SEM and TEM study the central part of all the samples are

TABLE III Phases found in the Al–Ni–Ti alloys by use of TEM

	Structure	Space group	Cell dimensions (nm)			Found in
			a	b	c	sample
$Al_{67}Ni_8Ti_{25}$	Au_3CU (Ll_2)	Pm $\bar{3}$ m	0.394			B, C, D, E
Al_2NiTi	$Mn_{23}Th_6$	Fm $\bar{3}$ m	1.190			B, C, D, E
Al_3NiTi_2	$MgZn_2$	$P6_3/mmc$	0.498		0.812	D, E
Al_3Ni	Al_3Ni	Pmn$\bar{a}$	0.66114	0.73662	0.48117	A
AlNi	CsCl	Pm $\bar{3}$ m	0.28864			B, C
Al_3Ti	Al_3Ti (DO_{22})	I4/mmm	0.3848		0.8596	A
$AlNTi_2$	$AlCCr_2$	$P6_3/mmc$	0.299		1.361	B, C, D, E
Al–Ti precip.		Tetragonal prim.	0.39		1.18	B

characterised by small dendrites and Ni-rich phases in the interdendritic regions. In the following the laser process and the resulting microstructure characteristics of the Al–Ni–Ti alloys will be discussed and compared to previous reports on more conventionally processed Al–Ni–Ti alloys.

5.1. The laser process

The laser process is a fast and easy method for producing small quantities of intermetallic material. In addition the laser process may be used for surface treatments and surface modifications of intermetallic phases [30]. However, the laser processing is unsuitable for producing materials for large-scale mechanical testing because of the small amount of material produced.

As shown in the present study, the laser process results in rapidly solidified alloys with a homogeneous distribution of the elements in the fully melted parts of the samples. Because of shorter diffusion distances in the fine microstructure of rapidly solidified alloys one needs much shorter homogenisation times compared to conventionally solidified alloys [31]. Ma *et al.* [14] used homogenisation time of 100 h at 1000 °C as used for arc-melted alloys [16, 32]. This homogenisation time is usually too long, and homogenisation time about one order of magnitude less is expected to be enough. Because the dimensions of the melted alloys are very small, too-long homogenisation times can introduce severe oxidation. This problem might be less important if one works with less active elements.

5.2. The DO_{22}–$L1_2$ phase transformations and precipitation in the $L1_2$ phase

The DO_{22}, DO_{23} and the $L1_2$ structure are related with antiphase shifts on the a–b planes. At 800 °C the transformation from the DO_{22}-type structure to the $L1_2$-type structure is expected to occur via the DO_{23} type structure with increasing Ni content, according to the phase diagram of Raman *et al.* [18]. As pointed out earlier the $Al_{11}Ti_5$ phase with the DO_{23} structure was not found in any of the processed alloys. The DO_{23} structure was reported by Raman *et al.* [18] in two Al–Ni–Ti alloys with 3 and 6 at. % Ni and 25 at. % Ti. The $Al_{69}Ti_{25}Ni_6$ alloy, which had been homogenised at 700 °C for 7.5 days, contained 30% of the DO_{23} structure and 50% of the $L1_2$ structure. In a more recent investigation by Mazdiyasni *et al.* [32] of seven Al-rich Al–Ni–Ti alloys, including the $Al_{69}Ti_{25}Ni_6$ composition, no evidence of the DO_{23} structure was found. The alloys were heat-treated at 1200 °C for 500 h, and an equilibrium-phase diagram for the Al-rich corner was drawn. The dendritic phases in the present Al–Ni–Ti alloys are consistent with the equilibrium-phase diagram at 1200 °C.

In the study of Mazdiyasni *et al.* [32] the $L1_2$ phase field was found to be larger at 1200 °C compared to 800 °C as found by Raman *et al.* [18]. The $L1_2$ phase field was found to shift towards higher Al-content with Ni composition ranging from 6–10 at. % at 25 at. % Ti. The decrease in the width of the $L1_2$ phase field as the temperature drops from 1200 to 800 °C results in the formation of precipitates within the $L1_2$ phase [32].

In recent years several observations of precipitates in modified Al_3Ti alloys with the $L1_2$ structure have been reported [9, 10, 33–38]. The precipitates are commonly referred to as Al_2Ti. In the present work the precipitates were found in the central parts of the dendrites in Alloy B. These regions have low-Ni content and relatively high-Ti content compared to the outer part of the dendrites (Table II). This indicates that the precipitates in the present study are of the same kind as previously reported in the literature.

Several different structures of the Al_2Ti phase have been published [35, 39–42]. In binary Al–Ti alloys two different structures of the Al_2Ti phase have been described with the Ga_2Hf and Ga_2Zr type structures [39–41]. In recent works by Yang and Goo [35, 42] two new types of Al_2Ti have been described precipitating out in $Al_{64}Fe_8Ti_{28}$ with the $L1_2$ structure. The tetragonal primitive Bravias lattice of the precipitates identified in the present study has, however, not been reported by others. The different stacking sequence found in the ternary alloying systems is expected to be dependent on the alloying element M.

5.3. Reports on interdendritic phases in Al–Ni–Ti alloys

In agreement with previous reports [10, 16–18] the main interdendritic phase is Al_2NiTi when the Ni content is between 8 and 15 at. % Ni (Alloy B–E). In alloys with 3 and 6 at. % Ni, Raman *et al.* [18] found Al_3Ni_2 together with Al_3Ti (DO_{22}) and $L1_2/DO_{23}$ respectively. The Al_3Ni_2 phase was also found by Nakayama and Mabuchi [43] and Biswas and Varin [10] in as cast alloys with 8–12 at. % Ni. The phase did, however, disappear during the homogenisation at 1000 °C for 100 h.

The Al_3Ni_2 phase was not found in the present study but three other intermetallics containing Ni were found. As seen from Table III, Al_3Ni was found in Alloy A, whereas AlNi was found in Alloy B and C. Al_3NiTi_2 was found in Alloy D and E. As shown in Fig. 4a the $AlNTi_2$ needles are also an interdendritic phase. As pointed out earlier, the $AlNTi_2$ needles are found to a large extent in Alloy B and to a smaller extent in Alloy D–E. The length of the needles in Alloy B is about 40 μm.

5.4. The $AlNTi_2$ needles

The $AlNTi_2$ phase has been reported only to exist in Al-rich AlTi by Kaufman *et al.* [44], and more recently it was found by Wu *et al.* [45] to exist in Ll_2 Al_3Ti-based alloys macroalloyed with Fe. Several different cell dimensions of the phase have been reported. Loiseau and Lasalmonie [46] found from HREM images the cell dimensions to be $a = 0.30$ nm and $c = 1.40$ nm whereas Kaufman *et al.* [44] and Wu *et al.* [45] found $a = 0.304$ nm and $c = 1.389$ nm and $a = 0.2995$ and $c = 1.361$ nm, from SAD and X-ray diffraction (XRD) respectively. Earlier XRD work on the Al–Ti–N system by Jeischko *et al.* [28] and Schuster and Bauer [47] reports the cell dimensions $a = 0.2994$ nm and $c = 1.361$ nm and $a = 0.29912$ and $c = 1.3621$ nm, respectively.

In the literature an Al–Ti phases based on α–Ti with a hcp structure and space group $P6_3/mmc$ [48, 49] has been described. The cell dimensions of the Al–Ti phase has been reported by Rostoker [50], McHargue *et al.* [51] and Clark *et al.* [52] to change non-linearly with composition. The cell dimensions in the composition range $x = 0 - 0.4$ were reported by Rostoker [50] to be $a = 0.2944 - 0.2877$ nm and $c = 0.4679 - 0.4612$ nm. In the composition range $x = 0 - 0.15$ the cell dimensions were reported to be $a = 0.2950 - 0.2900$ nm and $c = 0.4683 - 0.4645$ nm [51] and $a = 0.2955 - 0.2925$ nm and $c = 0.4685 - 0.4667$ nm [52].

The structure of the $AlNTi_2$ phase is closely related to this Al–Ti phase and can be described with three times the c-axes of the α–Ti-based structures (MoS_2 type of structure) with interstitial N planes intersecting at $z = 0, 1/2$ ($AlCCr_2$ type of structure).

Needles can be seen both directly after the laser processing and after homogenisation at 1000 °C in the work by Ma *et al.* [14]. The needles are probably of the same kind as found in the present work. Because the needles remain present after homogenisation at 1000 °C for 100 h, they are expected to be very stable at high temperatures. This is in agreement with the findings of Wu *et al.* [45] who found the $AlNTi_2$ phase present after annealing at 1100 °C for 60 hours and after arc-melting a specimen 5 times.

The shape of the $AlNTi_2$ phase was by Wu *et al.* [45] found to be of two types: ribbonlike and rectangular precipitates. The rectangular precipitates were expected to form in the liquid before the $L1_2$, whereas the ribbonlike seemed to have formed during the solidification. In the present investigation the $AlNTi_2$ phase has been found in connection with the interdendritic regions. Therefore it is expected that the $AlNTi_2$ phase is formed after the $L1_2$ dendrites. One should, however, keep in mind that the present samples have been rapidly cooled in contrast to the samples investigated by Wu *et al.* [45].

The needles in alloy B are found to contain a small dislocation in the tip as seen from BF images (Fig. 9). One can also see a contrast difference in the middle of the needle (Fig. 9), which can be interpreted as a hollow core. The existence of a hollow core and the dislocation in the tip of the needle support the theory that the needles are growing with a screw dislocation mechanism. This screw mechanism has earlier been described by Sears [53, 54] for mercury, based on a theory of crystal growth proposed by Frank [55] and Burton *et al.* [56].

It is expected that N in the air is the source of the N found in the needles. The cold-pressed samples are porous, and air can be trapped in the pores. Even though the samples are blown with He during the laser processing, it is possible that trapped N can react with the molten Al and Ti, resulting in the $AlNTi_2$ phase.

6. Conclusion

We have presented a comprehensive study of the microstructure of laser-processed $(Al_{1-x}Ni_x)_3Ti$ with Ni content ranging from 5 to 15 at. %. The laser-process method was found to be suitable for producing small quantities of intermetallic materials for structural and phase-relation studies. The cooling rate of the processing method was found to be of the order of 10^3 K/s.

The dendrites in the 5 at. % Ni alloy consisted of the Al_3Ti phase with the DO_{22}-type structure, whereas the remaining alloys consist of $Al_{67}Ni_8Ti_{25}$ phase with the $L1_2$-type structure. The lattice parameter of the $L1_2$ type structure $Al_{67}Ni_8Ti_{25}$ was determined by comparing the Higher Order Laue Zone (HOLZ) line patterns in experimental and calculated convergent beam electron diffraction disks. The lattice parameter was found to be $a = 0.3935 \pm 0.0003$ nm.

In the $L1_2$ structure in the alloy with 8 at. % Ni, Al_2Ti precipitates with a new primitive tetragonal structure were found. The cell dimensions are $a = 0.39$ nm and $c = 1.18$ nm.

$AlNTi_2$ was found as needles in the interdendritic regions. The Ti : Al ratio of the phase was found to be 2.0 ± 0.2. The $AlNTi_2$ phase has a $AlCCr_2$-type structure, which can be related to the Al–Ti α–Ti-based structures with three times the c axis and interstitial N planes intersecting at $z = 0, 1/2$. The cell dimensions of the $AlNTi_2$ phase were in the present study found to be consistent with $a = 0.299$ nm and $c = 1.361$ nm.

Acknowledgements

This work was financially supported by the Norwegian Research Council. The authors would like to thank Svein Ove Olsen at SINTEF in Oslo for help with the laser processing of the samples.

References

1. M. YAMAGUCHI and Y. UMAKOSHI, *Prog. Mater. Sci.* **34** (1990) 1.
2. Y. UMAKOSHI, M. YAMAGUCHI, T. SAKAGAMI and T. YAMANE, *J. Mater. Sci.* **24** (1989) 1599.
3. M. YAMAGUSHI, Y. UMAKOSHI and T. YAMANE, *Phil. Mag. A* **A55** (1987) 301.
4. W. O. POWERS and J. A. WERT, *Phil. Mag. A* **60** (1989) 585.
5. J. P. NIC, S. ZHANG and D. E. MIKKOLA, *Scripta Metall. et Mater*. **24** (1990) 1099.
6. W. O. POWERS and J. A. WERT, *Metall. Trans. A* **21A** (1990) 145.
7. N. DURLU and O. T. INAL, *J. Mater. Sci.* **27** (1992) 3225.
8. R. LERF and D. G. MORRIS, *Acta Metall. et Mater*. **42** (1994) 1091.
9. Z. L. WU, D. P. POPE and V. VITEK, *Phil. Mag. A* **70** (1994) 159.
10. S. BISWAS and R. A. VARIN, *Metall. Mater. Trans. A* **27A** (1996) 5.
11. E. P. GEORGE, J. A. HORTON, W. D. PORTER and J. H. SCHNEIBEL, *J. Mater. Res*. **5** (1990) 1639.
12. C. L. FU, *J. Mater. Res*. **5** (1990) 971.
13. E. A. FEEST and J. H. TWEED, in *High Temperature Intermetallics* (Royal Society, London, 1991), p. 30.
14. Y. MA, T. ARNESEN, J. GJØNNES and J. TAFTØ, *J. Mater. Res.* **7** (1992) 1722.
15. U. PRAKASH, R. A. BUCKLEY, H. JONES and C. M. SELLAR, *J. Mater. Sci*. **27** (1992) 2001.
16. C. D. TURNER, W. O. POWERS and J. A. WERT, *Acta Metall*. **37** (1989) 2635.
17. S. C. HUANG, E. L. HALL and M. F. X. GIGLIOTTI, *J. Mater. Res.* **3** (1988) 1.
18. A. RAMAN and K. SCHUBERT, *Z. Metallkd.* **56** (1965) 99.
19. M. C. FLEMMING, in *Materials Science and Technology: Processing of Metalls and Alloys*, edited by R. W. Chan, P. H. Haasen and E. J. Kramer. (VCH Verlagsgesellschaft mbH, 1991), Vol. 15, 1, 57.
20. G. BRAUER, *Z. Anorg. Allg. Chem.* **242** (1939) 1.
21. K. SCHUBERT, H. G. MEISSNER, A. RAMAN and W. ROSSTEUTSCHER, *Naturwisserschaften* **51** (1964) 287.
22. N. DURLU and O. T. INAL, *J. Mater. Sci.* **27** (1992) 1175.
23. R. HØYER, *Acta Cryst.* **A25** (1969) 516.
24. A. OLSEN, *J. Appl. Cryst.* **9** (1976) 9.
25. K. GODWOD, R. KOWALCZYK and Z. SZMID, *Phys. Status Solidi (a)* **21** (1974) 227.
26. A. J. BRADLEY and A. TAYLOR, *Phil. Mag.* **23** (1937) 1049.
27. M. COOPER, *Phil. Mag.* **8** (1963) 811.
28. V. Y. MARKIV, V. V. DURNASHOVA and V. R. RYABOV, *Metallofizika* **46** (1973) 103.
29. W. JEITSCHKO, H. NOWOTNY and F. BENSOVSKY, *Monatsh. Chem.* **94** (1963) 1198.
30. W. JEITSCHKO, H. NOWOTNY and F. BENSOVSKY, *Monatsh. Chem.* **94** (1963) 672.
31. L. GJØNNES and A. OLSEN, *J. Mater. Sci.* **29** (1994) 728.
32. J. D. VERHOEVEN, *Fundamentals of physical metallurgy* (John Wiley and Sons, inc., 1975), 279, 316.
33. S. MAZDIYASNI, D. B. MIRACLE, D. M. DIMIDUK, M. G. MENDIRATTA and P. R. SUBRAMANIAN, *Scripta Metall.* **23** (1989) 327.
34. C. T. FORWOOD and M. A. GIBSON, *Mat. Sci. Forum* **189-190** (1995) 353.
35. D. G. MORRIS, R. LERF and M. LEBOEUF, *Mat. Res. Soc. Symp. Proc.* **364** (1995) 1215.
36. T. Y. YANG and E. GOO, *Metall. Mater. Trans. A* **26A** (1995) 1029.
37. K. S. KUMAR, M. S. DIPIETRO and J. D. WHITTENBERGER, *Acta Metall. et Mater.* **5** (1993) 1379.
38. D. G. MORRIS and S. GUNTER, *Acta Metall. et Mater.* **40** (1992) 3065.
39. L. POTEZ, A. LOISEAU, S. NAKA and G. LAPASSET, *J. Mater. Res*. **7** (1992) 876.
40. M. POLZSCHKE and K. SCHUBERT, *Z. Metallkde*. **53** (1962) 548.
41. A. LOISEAU and C. VANNUFFEL, *Phys. Status Solidi (a)* **107** (1988) 655.
42. J. C. SCHUSTER and H. IPSER, *Z. Metallkde*. **81** (1990) 389.
43. T. Y. YANG and E. GOO, *Metall. Mater. Trans. A* **25A** (1994) 715.
44. Y. NAKAYAMA and H. MABUCHI, *Intermetallics* **1** (1993) 41.
45. M. J. KAUFMAN, D. G. KONITZER, R. D. SHULL and H. L. FRASER, *Scripta Metall*. **20** (1986) 103.
46. Z. L. WU, D. P. POPE and V. VITEK, *Metall. Mater. Trans. A* **26A** (1995) 521.
47. A. LOISEAU and A. LASALMONIE, *Mater. sci. Eng.* **67** (1984) 163.
48. J. C. SCHUSTER and J. BAUER, *J. Solid State Chem.* **53** (1984) 260.
49. R. R. PAWAR and V. T. DESHPANDE, *Acta Cryst*. **A24** (1968) 316.
50. N. SCHMITZ-PRANGHE and P. DUNNER, *Z. Metallkd*. **59** (1968) 377.
51. W. ROSTOKER, *Trans. AIME* **194** (1952) 212.
52. C. J. MCHARGUE, S. E. ADAIR and J. P. HAMMOND, *Trans. AIME* **197** (1953) 1199.
53. D. CLARK, K. S. JEPSON and G. I. LEWIS, *J. Inst. Metals* **91** (1963) 197.
54. G. W. SEARS, *Acta Metall*. **1** (1953) 457.
55. G. W. SEARS, *Acta Metall*. **3** (1955) 361.
56. F. C. FRANK, *Disc. Faraday soc.* **5** (1949) 48.
57. W. K. BURTON, N. CABERA and F. C. FRANK, *Phil. Trans. Roy. Soc. London, Ser. A* **243** (1951) 299.

Received 22 November 1997
and accepted 15 July 1998